Extended Look-Ahead Tracking Controller With Orientation-Error Observer for Vehicle Platooning

Anggera Bayuwindra, Erjen Lefeber, Jeroen Ploeg, and Henk Nijmeijer, *Fellow, IEEE*

***Abstract*— This paper presents a novel extended look-ahead concept of an integrated lateral and longitudinal vehicle following controller with an orientation-error observer. The control law is based on input-output feedback to address a local tracking problem. It is known that due to the position control in the look-ahead approach, the follower vehicle may cut corners. To address this problem, a reference-induced extended look-ahead tracking point is introduced such that the cutting-corner is compensated. Moreover, the stability of the internal dynamics is analyzed. To address the situation where the orientation tracking error is not measurable or corrupted by noise, an orientation-error observer, constructed from the position tracking error, is designed. The performance of the extended look-ahead controller and the orientation-error observer is investigated by means of a simulation study, and validated with experiments on a mobile robot platform.**

***Index Terms*— Control algorithm, vehicle platooning, observer, cascaded system, longitudinal and lateral control.**

I. Introduction

IN RECENT years, the increasing needs for mobility has caused a high need of transportation. One solution to compensate for the increasing number of vehicles is to develop more infrastructure or to increase the capacity of existing infrastructure. Since the development of the infrastructure is time consuming, costly, and infeasible in some situations, increasing highway capacity is seen as the most effective solution. One of the methods to increase the highway capacity is vehicle platooning. With the concept of automated vehicles, platooning allows a vehicle to drive closer to its preceding vehicle by eliminating the reaction time of human driver. The concept of vehicle platooning in longitudinal movement is realized through Cooperative Adaptive Cruise Control (CACC). CACC, as an extension of ACC, utilizes wireless communications between vehicles (V2V communication) so that acceleration information of the preceding vehicle can be used as a feed-forward term to attenuate disturbances along the platoon [1]. This is an advantage of CACC over ACC, whereas the disturbance in ACC may be amplified in the upstream direction [2]. For lateral movement, vehicle platooning control can be designed by two main approaches, i.e., a path following approach and a trajectory tracking approach. In path following, the control objective is to drive the vehicle over a desired path without any time constraint, i.e., there is no requirement of when the vehicle should arrive at a certain point. Since there is no time requirement, the vehicle's longitudinal velocity can be freely regulated, independent of the position on the spatial path [3]. On the other hand, in the trajectory tracking approach, the desired path is parameterized with respect to time, i.e., the vehicle is required to be at a specific position along the path at a specific time.

In [4], a lane keeping controller based on the path following approach, is designed such that the vehicle follows a reference path, e.g., the path composed of lane markings (either road surface or embedded magnetic markings) using a camera or magnetic sensor, known as a "look-down" technique. It should be noted that the term "look-down" is rather loose since the vehicle also requires to look for the lane markings in front of it. The control objective of a lane keeping is to design a steering input that brings the lateral error, i.e., distance from the vehicle's position to the path, to zero. Most path following methods address the control problem by assigning the motion along a path in a single coordinate. The single intrinsic coordinate system used in the path following itself is known as a Serret-Frenet reference frame, where the origin is determined by the projection of the vehicle [3]. The projection of the vehicle's position onto the path is then used as reference for the control problem. The research in [5] has shown that the orthogonal projection with respect to the path has a local character in the sense that the vehicle has at first to get to the desired path orthogonally before it can project itself on the path. Since in the Serret-Frenet frame the longitudinal distance has been transformed into a curvilinear distance, the longitudinal control then can be realized through CACC. The combination of a lane keeping controller and CACC becomes a trajectory control problem, since there is a time requirement to be fulfilled. With this combined approach, the follower vehicles in a platoon drive in the exact same path as the leader vehicle, and the spacing distance objective can be fulfilled with the CACC controller [6]. However, the lane keeping performance in this approach relies heavily on the reference markers and V2I (vehicle-to-infrastructure) communication to provide the platoon with information about

Manuscript received September 4, 2018; revised February 28, 2019, July 16, 2019, and September 20, 2019; accepted October 2, 2019. Date of publication October 21, 2019; date of current version October 30, 2020. This work was supported by the Indonesian Ministry of Finance through the Indonesia Endowment Fund for Education under Grant S-218/LPDP/2013. The Associate Editor for this article was D. F. Wolf. *(Corresponding author: Anggera Bayuwindra.)*

A. Bayuwindra, E. Lefeber, and H. Nijmeijer are with the Mechanical Engineering Department, Eindhoven University of Technology, 5612 AZ Eindhoven, The Netherlands (e-mail: a.bayuwindra@tue.nl; a.a.j.lefeber@tue.nl; h.nijmeijer@tue.nl).

J. Ploeg is with 2getthere, 3543 AE Utrecht, The Netherlands, and also with the Department of Mechanical Engineering, Eindhoven University of Technology, 5612 AZ Eindhoven, The Netherlands (e-mail: jeroen@2getthere.eu).

Digital Object Identifier 10.1109/TITS.2019.2947348

road structure. From the viewpoint of vehicle platooning, the major disadvantage of the path following approach is when the inter-vehicle distance is getting small, the look-down system is unable to track the lane markings accurately as they are obstructed by the preceding vehicle [7].

As an alternative to lane keeping, a direct vehicle-following control is designed. A direct vehicle-following control uses the current preceding vehicle's position as a reference while keeping a desired distance. The vehicle-following control of vehicle platoons was developed from CACC and was first designed for a longitudinal control [8]–[10]. In this approach, the follower vehicle tracks the current position of the preceding vehicle by using a camera (or lidar) and determines the relative distance with respect to the follower vehicle, commonly known as a "look-ahead" technique. The vehicle-following control was then extended to both longitudinal and lateral control in [11]–[13]. The objective of this longitudinal and lateral vehicle-following control is to minimize the error between the measured relative distance and the desired distance (e.g., spacing policy in CACC), and to minimize the lateral error with respect to the preceding vehicle's path. One of the main challenges in this approach is to determine the path of the preceding vehicle. Since the follower vehicle can only measure the distance as a straight line (as opposed to the curvilinear distance in the Serret-Frenet frame), the follower vehicle can deviate from the path of the preceding vehicle during cornering, known as corner cutting. In [12], a reference virtual point, which is positioned at a desired known distance behind the lead vehicle, is proposed to compensate the corner cutting. The results shows that the proposed solution was able to compensate the corner cutting for the path with small curvatures, but was ineffective for the path with large curvatures. In [14], an extended look-ahead approach has been designed, based on dynamic feedback linearization, to compensate for the corner cutting. The extended look-ahead uses the velocity and heading information of the preceding vehicle (which are available from radar and V2V communication) to create a virtual reference-induced look-ahead point as a new tracking objective for the follower vehicle. The results are then elaborated in [15] with the formal stability analysis, where the stability of the internal dynamics is guaranteed under bounded curvatures, lateral jerk, and acceleration of the preceding vehicle. The error dynamics in [14], [15] are defined as a global tracking problem, in which the position and orientation of each vehicle is assumed to be measurable with respect to a global (i.e., fixed) coordinate frame. The shortcoming of this method is that the global position and orientation of vehicles are commonly not available in practical situations.

The main contribution of this paper is the design of the extended look-ahead controller as a local tracking problem, where the error dynamics are defined with respect to the target position of the follower vehicle. The advantage of our proposed controller to the path-following control (e.g., [3], [5]) is that it does not need lane markings and utilizes the already available information from CACC setup, thus providing benefits for a practical implementation and cost-efficiency. To study the internal dynamics of the resulting system, a formal stability analysis is provided. Moreover, the control strategy is then further extended with an orientation-error observer, addressing the situation where the relative orientation between vehicles is not measurable, or corrupted by noise. The effectiveness of the extended look-ahead controller against corner-cutting is demonstrated by a simulation case study, and further validated by an experiment with mobile robots.

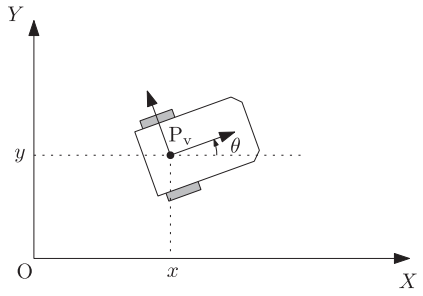

Fig. 1. A unicycle mobile robot in Cartesian coordinates.

The organization of this paper is as follows: Section II presents the concept of the extended look-ahead control design for vehicle platoons, starting with the problem formulation. The extended look-ahead controller is proposed, and a stability analysis is subsequently provided. Section III presents the design of the orientation-error observer. The results of the simulation study are presented in Section IV. For further validation, the extended look-ahead controller and the orientation-error observer are implemented in a mobile robot platform in Section V. Finally, the concluding remarks are discussed in Section VI.

II. Control of Vehicle Platooning With Extended Look-Ahead

A. Problem Formulation

Consider a unicycle-type vehicle with the posture $[x(t), y(t), \theta(t)]^T$ (see Fig. 1) that can be described by following differential equations

$$\dot{x} = v\cos\theta \tag{1a}$$

$$\dot{y} = v\sin\theta \tag{1b}$$

$$\dot{\theta} = \omega, \tag{1c}$$

where $\mathrm{P_v} = (x, y)$ are the Cartesian coordinates of the axle center of the vehicle, θ is the orientation of the vehicle with respect to the global X axis, v is the linear velocity input and ω is the angular velocity input of the vehicle.

Consider a reference vehicle with the posture $[x_r(t), y_r(t), \theta_r(t)]^T$ and the kinematics given by

$$\dot{x}_r = v_r\cos\theta_r \tag{2a}$$

$$\dot{y}_r = v_r\sin\theta_r \tag{2b}$$

$$\dot{\theta}_r = \omega_r, \tag{2c}$$

where (x_r, y_r) are the Cartesian coordinates of the axle center of the reference vehicle, θ_r is the orientation of the reference vehicle with respect to the global X axis, v_r and ω_r are the reference velocity and angular velocity

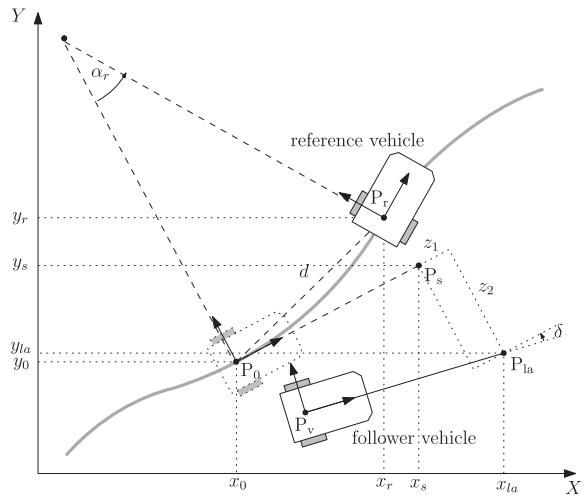

Fig. 2. Trajectory tracking problem with extended look-ahead, where $|P_0P_r| = |P_0P_s| = d$.

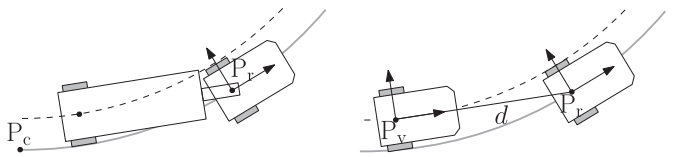

Fig. 3. Analogy of cutting corner in a truck with trailer (left) and in a vehicle platooning (right). The solid gray line is a path traveled by the leader vehicle/truck, while the dashed black line is a path traveled by the follower vehicle/container.

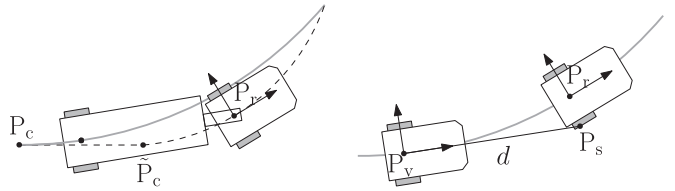

Fig. 4. Compensation of the cutting corner problem in a truck with container (left), and in a vehicle platooning (right).

input, respectively. The trajectory tracking problem is typically solved by stabilizing the position of P_v with respect to the reference P_r and orientation of θ with respect to the reference orientation θ_r. The relative kinematics between these points can be determined with respect to the follower vehicle frame (e.g., see [16]–[19]), the reference vehicle frame (e.g., see [3], [12]), or any moving frame, which results in different error dynamics. In our approach, we choose the relative kinematics with respect to the frame of the desired posture of the follower vehicle. This choice makes the mathematical development easier than other frame choices, as explained in the next section.

Now consider a trajectory tracking problem with a look-ahead distance (referred as a vehicle-following control problem), in which the objective of the follower vehicle is to follow the reference vehicle at a desired distance d. We define P_0 as a target point of the follower vehicle, and P_{la} as a look-ahead point attached to the follower vehicle. The coordinates of P_{la} are defined as

$$x_{la} = x + d\cos\theta \tag{3a}$$

$$y_{la} = y + d\sin\theta, \tag{3b}$$

where (x, y) are the Cartesian coordinates of the follower vehicle, $|P_0P_r| = d$, and the distance $d \in \mathbb{R}_+$ (see Fig. 2). With this look-ahead point, the control objective of the vehicle following problem could then be to stabilize at zero the tracking errors $(x_{la} - x_r, y_{la} - y_r)$ of that point P_{la} with respect to the reference point P_r. However, in a curve, the leader-follower vehicle system has a unique instantaneous center of rotation (ICR), such that the line through the axle of each unicycle goes through this ICR. Consequently, when (x_{la}, y_{la}) have converged to (x_r, y_r), the follower vehicle will drive at a shorter distance to the ICR, i.e., it will cut corners [12], [14]. It is interesting to remark that this problem is analogous to a truck-trailer combination, see Fig. 3. On cornering maneuvers, a trailer coupled to the truck will also have the cutting-corner problem and human drivers solve this problem by letting the truck turn at the point in front of the cornering point, denoted by $\tilde{P}_c$, such that the trailer will travel on the desired arc, see Fig. 4(left).

Based on the same approach, we extend the look-ahead point in our error dynamics, thus creating a "reference-induced look-ahead point" as the new tracking point objective (denoted by P_s) for the follower vehicle such that cutting corner can be compensated. The position of P_s in the Cartesian coordinate system is defined by (x_s, y_s) and formulated such that the distance of $|P_vP_s|$ equals the look-ahead distance d (Fig. 4(right)). In other words, the "reference-induced look-ahead point" P_s can be regarded as the position of where the look-ahead point P_{la} should be. With this new look-ahead point P_s, our control objective is then to stabilize at zero the tracking errors $(x_{la} - x_s, y_{la} - y_s)$, see Fig. 2. Before we define the tracking error, first we shall derive the position of P_s geometrically based on the position of reference vehicle P_r.

B. Derivation of the Reference-Induced Look-Ahead Point P_s

To derive the position of P_s, let us first denote P_0 as a moving origin point, where (x_0, y_0) is the position of P_0 in the Cartesian coordinate system, θ_0 is the angle with respect to the global X axis, and $|P_0P_r| = d$. This point P_0 can also be considered as the position of where the follower vehicle P_v should be. Define α_r as the angle of the circular arc formed by P_0 and P_r, see Fig. 5. To derive the angle α_r, let us denote κ_r as the curvature of the reference vehicle, which is defined as

$$\kappa_r := \frac{\mathrm{d}\theta_r}{\mathrm{d}s_r} = \left(\frac{\mathrm{d}\theta_r}{\mathrm{d}t}\right) / \left(\frac{\mathrm{d}s_r}{\mathrm{d}t}\right) = \frac{\omega_r}{v_r}, \tag{4}$$

where $v_r \neq 0$, θ_r is the orientation of the reference vehicle (which can also be considered as the angle of the tangent to the curve or path), and s_r is the curvilinear coordinate. On a curved path, it can be observed that d characterizes the chord length of a circular segment formed by P_0 and P_r, and the angle α_r can be defined as

$$\alpha_r = 2\arcsin\left(\frac{1}{2}d\kappa_r\right), \tag{5}$$

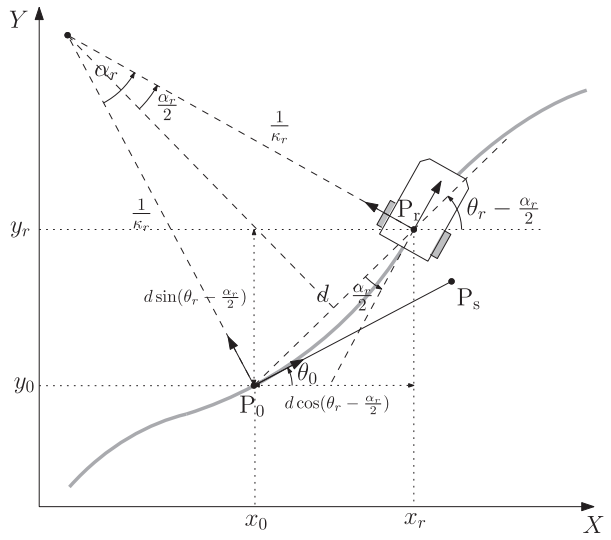

Fig. 5. Projection of the reference-induced look-ahead point P_s.

where $|\kappa_r| \leq \kappa^{\max} < 1/d$, and $\kappa^{\max}$ is a constant, maximum value of the curvature of the reference vehicle. It should be noted that α_r is defined as a function of the curvature κ_r of the reference vehicle, which fully determines the circular arc. Thus, it is not a circular arc through any two arbitrary points, but it is an arc through the position of P_r with a known curvature. By noting that (see Fig. (5))

$$\sin\frac{\alpha_r}{2} = \frac{1}{2}d\kappa_r, \quad \cos\frac{\alpha_r}{2} = \frac{\sqrt{4-d^2\kappa_r^2}}{2}, \tag{6}$$

the derivative of α_r with respect to time is obtained as

$$\dot{\alpha}_r = \frac{2d}{\sqrt{4-d^2\kappa_r^2}}\dot{\kappa}_r. \tag{7}$$

Since the length of P_0P_r equals the desired inter-vehicle distance d, the position of P_0 in a global Cartesian coordinate system can be defined as

$$x_0 = x_r - d\cos\left(\theta_r - \frac{\alpha_r}{2}\right) \tag{8a}$$

$$y_0 = y_r - d\sin\left(\theta_r - \frac{\alpha_r}{2}\right). \tag{8b}$$

First we define the rotation matrix as

$$R(\theta) = \begin{bmatrix}\cos\theta & -\sin\theta \\ \sin\theta & \cos\theta\end{bmatrix}. \tag{9}$$

From Fig. 5, it can be observed that the coordinate of P_s can be obtained by a rotation of $-\frac{\alpha_r}{2}$ from the coordinate P_r around (x_0, y_0) as

$$\begin{bmatrix}x_s \\ y_s\end{bmatrix} = \begin{bmatrix}x_0 \\ y_0\end{bmatrix} + R^T\left(\frac{\alpha_r}{2}\right)\begin{bmatrix}x_r - x_0 \\ y_r - y_0\end{bmatrix}. \tag{10}$$

By substituting (8) into (10), applying the angle sum formula, and noting that $R(\theta_r - \alpha_r) = R(\theta_r)R^T(\alpha_r)$, we can eventually rewrite (10) as

$$\begin{bmatrix}x_s \\ y_s\end{bmatrix} = \begin{bmatrix}x_r \\ y_r\end{bmatrix} + d\begin{bmatrix}\cos(\theta_r - \alpha_r) - \cos\left(\theta_r - \frac{\alpha_r}{2}\right) \\ \sin(\theta_r - \alpha_r) - \sin\left(\theta_r - \frac{\alpha_r}{2}\right)\end{bmatrix}$$

$$\begin{bmatrix}x_s \\ y_s\end{bmatrix} = \begin{bmatrix}x_r \\ y_r\end{bmatrix} + d\,R(\theta_r - \alpha_r)\begin{bmatrix}1 - \cos\frac{\alpha_r}{2} \\ -\sin\frac{\alpha_r}{2}\end{bmatrix}, \tag{11}$$

where $R(\theta_r - \alpha_r)$ as the rotation matrix through an angle $\theta_r - \alpha_r$. It can be observed that the position of the reference-induced look-ahead point P_s depends on the position of the reference vehicle P_r, the angle α_r, and the angle $\theta_r - \alpha_r$, which in fact, is the desired orientation of the follower vehicle. On a straight path, $\alpha_r = 0$, thus P_s will be equal to P_r. In the following section, we define the error dynamics with the extended look-ahead approach.

C. Error Dynamics and Controller Design of the Extended Look-Ahead

We consider the trajectory tracking problem between P_{la} and P_s, expressed in the frame of the desired posture of the follower vehicle, with origin P_0. It should be noted that we define the relative kinematics with respect to this particular frame because we want to cancel the rotation matrix $R(\theta_r - \alpha_r)$ factor in (11). Hence, the error state components are defined as

$$\begin{bmatrix}z_1 \\ z_2\end{bmatrix} = R^T(\theta_r - \alpha_r)\begin{bmatrix}x_{la} - x_s \\ y_{la} - y_s\end{bmatrix}, \tag{12}$$

with $x_{la} = x + d\cos\theta$, $y_{la} = y + d\sin\theta$, and $[x_s, y_s]^T$ as described in (11). It can be seen directly that $[z_1, z_2]^T$ denotes the relative position error. To obtain the error dynamics, we start first by differentiating $[z_1, z_2]^T$ with respect to time and taking (11) and (5) into account, resulting in

$$\begin{bmatrix}\dot{z}_1 \\ \dot{z}_2\end{bmatrix} = (\omega_r - \dot{\alpha}_r)\begin{bmatrix}z_2 \\ -z_1\end{bmatrix} + \begin{bmatrix}\cos\delta & -d\sin\delta \\ \sin\delta & d\cos\delta\end{bmatrix}\begin{bmatrix}v \\ \omega\end{bmatrix}$$
$$- \begin{bmatrix}\cos\alpha_r \\ \sin\alpha_r\end{bmatrix}v_r - \begin{bmatrix}\sin\frac{\alpha_r}{2} \\ 1 - \cos\frac{\alpha_r}{2}\end{bmatrix}d\omega_r$$
$$+ d\dot{\alpha}_r\begin{bmatrix}\frac{1}{2}\sin\frac{\alpha_r}{2} \\ 1 - \frac{1}{2}\cos\frac{\alpha_r}{2}\end{bmatrix}, \tag{13}$$

where

$$\delta = \theta - \theta_r + \alpha_r. \tag{14}$$

By applying the double angle formula on $\sin\alpha_r$ and $\cos\alpha_r$, substituting (6) and (4) into (13), we eventually obtain the error dynamics as

$$\begin{bmatrix}\dot{z}_1 \\ \dot{z}_2\end{bmatrix} = (\omega_r - \dot{\alpha}_r)\begin{bmatrix}0 & 1 \\ -1 & 0\end{bmatrix}\begin{bmatrix}z_1 \\ z_2\end{bmatrix} - \begin{bmatrix}v_r \\ d\omega_r\end{bmatrix}$$
$$+ \begin{bmatrix}\cos\delta & -d\sin\delta \\ \sin\delta & d\cos\delta\end{bmatrix}\begin{bmatrix}v \\ \omega\end{bmatrix} + \begin{bmatrix}h_{\kappa,1} \\ h_{\kappa,2}\end{bmatrix}\dot{\kappa}_r \tag{15}$$

with

$$h_{\kappa,1} = \frac{d^3\kappa_r}{2\sqrt{4-d^2\kappa_r^2}}, \quad h_{\kappa,2} = \frac{4d^2 - d^2\sqrt{4-d^2\kappa_r^2}}{2\sqrt{4-d^2\kappa_r^2}}. \tag{16}$$

If the follower vehicle converges to its desired position, θ converges to $\theta_r - \alpha_r$. Hence, δ in (14) is, in fact, the angular error of the follower vehicle. It can be observed that error dynamics (15) consist of: a linear time-varying term multiplying $[z_1, z_2]^T$, since ω_r and $\dot{\alpha}_r$ are external time-varying parameters; and a nonlinear term multiplying inputs $[v, \omega]^T$, since δ is a state of the system. The objective now is to design control laws $[v, \omega]^T$ that asymptotically stabilize the system (15) at the origin, based on input-output feedback linearization in [20, Chapter 13], [21]. Since the matrix multiplying $[v, \omega]^T$ is invertible, by choosing the control inputs

$$\begin{bmatrix} v \\ \omega \end{bmatrix} = \begin{bmatrix} \cos\delta & \sin\delta \\ -\dfrac{1}{d}\sin\delta & \dfrac{1}{d}\cos\delta \end{bmatrix} \begin{bmatrix} -k_1 z_1 + v_r - h_{\kappa,1}\dot{\kappa}_r \\ -k_2 z_2 + d\omega_r - h_{\kappa,2}\dot{\kappa}_r \end{bmatrix}, \quad (17)$$

where $d > 0$, we obtain the closed-loop system as follows

$$\begin{bmatrix} \dot{z}_1 \\ \dot{z}_2 \end{bmatrix} = \begin{bmatrix} -k_1 & \omega_r - \dot{\alpha}_r \\ -\omega_r + \dot{\alpha}_r & -k_2 \end{bmatrix} \begin{bmatrix} z_1 \\ z_2 \end{bmatrix}. \quad (18)$$

Noted that by the input-output feedback linearization, we obtain a closed-loop system which is a linear time-varying (LTV) system. Hence, the Lyapunov stability criterion is used to prove the stability of the closed-loop system. By the choice of $k_1, k_2 > 0$, it can be directly verified that the origin of subsystem $[z_1, z_2]^T$ is exponentially stable by the Lyapunov function $V_{12}(z_1, z_2) = \frac{1}{2}z_1^2 + \frac{1}{2}z_2^2$ such that

$$\dot{V}_{12}(z_1, z_2) = -k_1 z_1^2 - k_2 z_2^2 < 0, \quad (19)$$

for $(z_1, z_2) \neq 0$, which means that $\dot{V}_{12}$ is negative definite in (z_1, z_2). Since, however, the model (1) is of third order and the error dynamics (15) are of second order, first-order internal dynamics are present. The internal dynamics are the unobservable part of the system dynamics that comply with the desired output, while the zero dynamics is the internal dynamics of the system when the system output is kept at zero by the input [20]. It should be noted that analyzing the (global) stability of the internal dynamics has a more generic meaning than only analyzing the stability of the zero dynamics. Therefore, in the next section we analyze the stability of the internal dynamics.

D. Stability Analysis of the Internal Dynamics

From Section II.C, it has been shown that the control law (17) exponentially stabilizes the second-order error dynamics, which leaves us with the first-order internal dynamics since the original model (1) is of third order. The first obvious choice for the internal state would be δ, since δ resembles the orientation error between the actual and the desired orientation of the follower vehicle. However, in a steady state condition, which implies that $z_1 = z_2 = 0$ and $\dot{\kappa}_r = 0$, this choice leads to two equilibrium points $\delta = 0$ and $\delta = \arctan[(-2d\kappa_r)/(d^2\kappa_r^2 - 1)]$, where the physical interpretation of these points is depicted in Fig. 6 (see Appendix A for the derivation). The posture (x_1, y_1, θ_1) is the stable equilibrium point, and can be considered as the correct posture of where the follower vehicle should be. On the other hand, (x_2, y_2, θ_2) is the unstable equilibrium point, and depends on the curvature of the preceding vehicle. Due to the curvature-dependence of this unstable equilibrium point, we decided to define z_3 such that the stable equilibrium point corresponds with $z_3 = 0$ and the unstable equilibrium point with $z_3 = \pi$ (see Fig. 7). To that end, we define

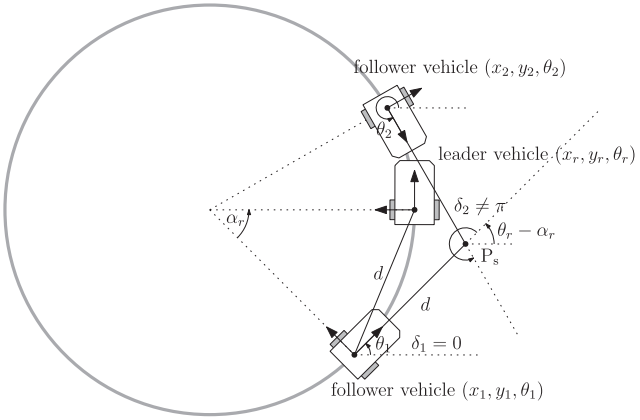

Fig. 6. Posture of the follower vehicle, (x_1, y_1, θ_1) and (x_2, y_2, θ_2), on two equilibrium points. In the stable equilibrium point (x_1, y_1, θ_1), $\delta_1 = 0$; and in the unstable equilibrium point (x_2, y_2, θ_2), $\delta_2 \neq 0 \neq \pi$.

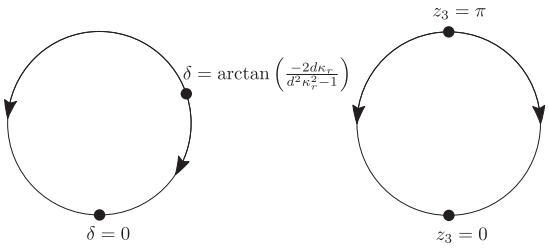

Fig. 7. The mapping of the equilibrium points from δ (left) to z_3 (right). By this mapping, the stable equilibrium point is at $z_3 = 0$; and the unstable equilibrium point maps to $z_3 = \pi$.

$$z_3 = \delta + \beta, \quad (20)$$

where the angle β is characterized by (see Appendix B for the derivation)

$$\sin\beta = \frac{d\kappa_r \cos\delta - d\kappa_r}{\sqrt{d^2\kappa_r^2(1-\cos\delta)^2 + (1 + d\kappa_r \sin\delta)^2}}, \quad (21a)$$

$$\cos\beta = \frac{1 + d\kappa_r \sin\delta}{\sqrt{d^2\kappa_r^2(1-\cos\delta)^2 + (1 + d\kappa_r \sin\delta)^2}}. \quad (21b)$$

where $|\kappa_r| \leq \kappa_r^{\max} < 1/d$. Note that from (20) and straightforward application of the trigonometric rules for the sum of angles, we have

$$\sin z_3 = \frac{\sin\delta + d\kappa_r(1-\cos\delta)}{\sqrt{d^2\kappa_r^2(1-\cos\delta)^2 + (1 + d\kappa_r \sin\delta)^2}}, \quad (22a)$$

$$\cos z_3 = \frac{\cos\delta + d\kappa_r \sin\delta}{\sqrt{d^2\kappa_r^2(1-\cos\delta)^2 + (1 + d\kappa_r \sin\delta)^2}}. \quad (22b)$$

Moreover, the derivative of β with respect to time follows from the inverse tangent function, derived from (21a) and (21b),

yielding

$$\dot{\beta} = \frac{d\dot{\kappa}_r \cos\delta - d\dot{\kappa}_r}{d^2\kappa_r^2 (1-\cos\delta)^2 + (1+d\kappa_r \sin\delta)^2} - \left(\frac{d\kappa_r \sin\delta + d^2\kappa_r^2 (1-\cos\delta)}{d^2\kappa_r^2 (1-\cos\delta)^2 + (1+d\kappa_r \sin\delta)^2}\right)\dot{\delta}. \quad (23)$$

Using (21), (22), (17), and noting the fact that $\dot{\delta} = \omega - \omega_r + \dot{\alpha}_r$, we obtain the derivative of z_3 with respect to time as

$$\begin{aligned}\dot{z}_3 &= \frac{d\dot{\kappa}_r \cos\delta - d\dot{\kappa}_r}{d^2\kappa_r^2 (1-\cos\delta)^2 + (1+d\kappa_r \sin\delta)^2} \\ &\quad + \left(\frac{d^2\kappa_r^2 (1-\cos\delta) + d\kappa_r \sin\delta + 1}{d^2\kappa_r^2 (1-\cos\delta)^2 + (1+d\kappa_r \sin\delta)^2}\right)\dot{\delta} \\ &= f_3(z), \end{aligned} \quad (24)$$

where

$$f_3(z) = -\frac{\bar{v}_r}{d}\sin z_3 + \xi_r \quad (25)$$

$$\bar{v}_r = \frac{N}{\sqrt{\Delta}} v_r \quad (26)$$

$$\xi_r = \frac{N}{\Delta}\left(\frac{k_1 \sin\delta}{d} z_1 - \frac{k_2 \cos\delta}{d} z_2\right) + g_\kappa \dot{\kappa}_r \quad (27)$$

$$N = d^2\kappa_r^2 (1-\cos\delta) + d\kappa_r \sin\delta + 1 \quad (28)$$

$$\Delta = d^2\kappa_r^2 (1-\cos\delta)^2 + (1+d\kappa_r \sin\delta)^2 \quad (29)$$

$$g_\kappa = \frac{N}{\Delta} f_r(\delta, d, \kappa_r) - \frac{d(1-\cos\delta)}{\Delta} \quad (30)$$

$$f_r(\delta, d, \kappa_r) = \frac{4d}{2\sqrt{4-d^2\kappa_r^2}} + \frac{d^2\kappa_r}{2\sqrt{4-d^2\kappa_r^2}}\sin\delta - \frac{4d - d\sqrt{4-d^2\kappa_r^2}}{2\sqrt{4-d^2\kappa_r^2}}\cos\delta, \quad (31)$$

$z = (z_1, z_2, z_3)$, $(N, \Delta) > 0$ (see (60) and (61) in Appendix C), and δ as in (14). It should be noted that (24) is a closed-loop system since the inputs (v, ω) have been taken into account. Thus, the overall closed-loop system is composed of (18) and (24), which is a third order system.

Remark 1: Note that since $|\kappa_r| \le \kappa_r^{\max} < 1/d$, $\bar{v}_r$ is lower- and upper-bounded by

$$|v_r| \le |\bar{v}_r| < \sqrt{2}\,|v_r|, \quad (32)$$

and $|\xi_r|$ is bounded by

$$|\xi_r| \le \frac{2+\sqrt{2}}{d} k_1 |z_1| + \frac{2+\sqrt{2}}{d} k_2 |z_2| + \frac{7d}{9}|\dot{\kappa}_r|. \quad (33)$$

Proof of (32) and (33): See Appendix C. ∎

Using these bounds on $|\bar{v}_r|$ and $|\xi_r|$, asymptotic stability of the internal dynamics (24) can be concluded by the following proposition.

Proposition 2: Consider the dynamics (24) where $\bar{v}_r$ and ξ_r are given in (26) and (27), respectively. Let $z_{12} = [z_1, z_2]^T$, and assume for all $t \ge 0$ that $0 < v_r^{\min} \le v_r(t)$, $|\kappa_r(t)| \le \kappa_r^{\max} < 1/d$, and $|\dot{\kappa}_r(t)| \le K$, where $d, K \in \mathbb{R}^+$.

1) *For $\varepsilon > 0$, if*

$$\|z_{12}(0)\| \le \frac{v_r^{\min}\varepsilon}{\left(2+\sqrt{2}\right)\sqrt{k_1^2 + k_2^2}}, \quad (34)$$

where $k_1, k_2 > 0$, then there exists t^* such that for $t \ge t^*$,

$$|\sin z_3(t)| \le \frac{7d^2}{9v_r^{\min}} K + \varepsilon. \quad (35)$$

2) *Moreover, if additionally*

$$\lim_{t\to\infty} \dot{\kappa}_r(t) = 0, \quad (36)$$

then $\lim_{t\to\infty} \sin z_3(t) = 0$.

3) *Finally, for $0 < \varepsilon < \frac{3}{10}$, if (34) holds,*

$$\cos z_3(0) \ge \sqrt{1 - \left(\tfrac{7}{18} - \tfrac{8}{27}\varepsilon\right)^2}, \quad (37)$$

and

$$|\dot{\kappa}_r(t)| \le K = \frac{v_r^{\min}}{d^2}\left(\frac{1}{2} - \frac{5}{3}\varepsilon\right), \quad (38)$$

we have $v(t) \ge \varepsilon v_r^{\min} > 0$ and $\lim_{t\to\infty} z_3(t) = 0$, rendering the internal dynamics (24) stable.

Proof: See Appendix D. ∎

Therefore, we can conclude that the internal dynamics (24), which correspond to the orientation of the vehicle, are stable under these conditions: the initial position error is not too large (bounded by (34)), the initial orientation error is bounded by (37), and the curvature derivative of the preceding vehicle is bounded by (38). Moreover, it is important to note that for a platoon with more than 2 vehicles, $v(t)$ will become the reference for the next vehicle. By Proposition 2(c), the requirement of $v(t) > 0$ is fulfilled for the initial condition $z_3(0)$ being bounded by (37) and $\dot{\kappa}_r(t)$ satisfying (38).

III. Orientation-Error Observer Design

From the previous section, it has been proven that the proposed controller design (17) guarantees that all error states (z_1, z_2, z_3) converge to zero, under the assumption that all states of the kinematic model are available and measurable for control. Here, the relative position (z_1, z_2) can be obtained from the camera or lidar, the preceding vehicle states (v_r, ω_r) can be obtained through wireless communication with the preceding vehicle, κ_r can be determined from v_r and ω_r, $\dot{\kappa}_r$ can be approximated by the backward Euler method, and δ is determined from the relative orientation $\theta - \theta_r$ and α_r, which may be measured using the camera. It is assumed that the relative position (z_1, z_2) can be measured accurately, and there is no delay involved in the wireless communication. In practical situations, there is often a case where the orientation of vehicles (θ, θ_r, or both) are not available, or disturbed by noise due to inherent limitations of the vision system. To address this problem, a state feedback controller combined with an observer that estimates the orientation was designed in [22], [23]. However, these approaches result in a combined observer-controller design which is different than the proposed tracking controller (17). Therefore, we adapt the observer designed in [23] by determining the orientation angle θ from the available states (z_1, z_2, v, ω) and design an observer such that the estimated angle (denoted by $\hat{\theta}$) converges to the actual orientation angle θ.

Consider the kinematic model of the unicycle as given in (1), and the available outputs as $[x, y]^T$. We extend the

dimension of the system (1) by defining new variables s and c as

$$s = \sin\theta, \quad c = \cos\theta, \tag{39}$$

which replace the orientation angle θ. As a result, we obtain the extended model of the unicycle as

$$\dot{x} = \upsilon c, \quad \dot{y} = \upsilon s, \tag{40a}$$

$$\dot{s} = \omega c, \dot{c} = -\omega s, \tag{40b}$$

where $[x, y]^T$ are the available outputs, $[\upsilon, \omega]^T$ are inputs, s and c as defined in (39). It should be noted that the transformation from the three-dimensional system (1) to four-dimensional system (40) introduces a constraint of the form $s^2 + c^2 = 1$.

Based on (40), an observer for x, y, c, and s can be defined as follows

$$\dot{\hat{x}} = \upsilon\hat{c} + l_1\zeta_x \tag{41a}$$

$$\dot{\hat{y}} = \upsilon\hat{s} + l_2\zeta_y \tag{41b}$$

$$\dot{\hat{c}} = -\omega\hat{s} + l_3\upsilon\zeta_x \tag{41c}$$

$$\dot{\hat{s}} = \omega\hat{c} + l_4\upsilon\zeta_y, \tag{41d}$$

where $l_1, l_2, l_3, l_4 > 0$, and $\zeta_x = x - \hat{x}$, $\zeta_y = y - \hat{y}$, $\zeta_c = c - \hat{c}$, and $\zeta_s = s - \hat{s}$ are the observer errors. Thus, we obtain the following observer error dynamics

$$\dot{\zeta}_x = \dot{x} - \dot{\hat{x}} = \upsilon\zeta_c - l_1\zeta_x \tag{42a}$$

$$\dot{\zeta}_y = \dot{y} - \dot{\hat{y}} = \upsilon\zeta_s - l_2\zeta_y \tag{42b}$$

$$\dot{\zeta}_c = \dot{c} - \dot{\hat{c}} = -\omega\zeta_s - l_3\upsilon\zeta_x \tag{42c}$$

$$\dot{\zeta}_s = \dot{s} - \dot{\hat{s}} = \omega\zeta_c - l_4\upsilon\zeta_y. \tag{42d}$$

It can be observed directly that if (42) converges to zero, then the estimated states $(\hat{x}, \hat{y}, \hat{c}, \hat{s})$ converge to (x, y, c, s). To prove stability of (42), the following proposition can be used.

Proposition 3 ([24], [25]): Consider the dynamics (42) with $l_1, l_2, l_3, l_4 > 0$. If υ, ω are bounded differentiable functions, $\dot{\upsilon}$ is bounded, and $0 < \upsilon_{\min} \leq \upsilon(t)$, then (42) is uniformly globally asymptotically stable (UGAS) at the origin.

Proof: See Appendix E. ∎

Using Proposition 3, we have that the origin of (42) is uniformly globally asymptotically stable (UGAS) and $\zeta_x(t)$, $\zeta_y(t)$, $\zeta_c(t)$, $\zeta_s(t)$ converge to zero as $t \to \infty$, subject to the necessary and sufficient condition of $\upsilon(t) > 0$ for all t [see Proposition 2(c)]. It remains to prove the convergence of the estimated orientation angle to the actual orientation angle θ. Define the estimated orientation angle $\hat{\theta}$ as

$$\hat{\theta} := \operatorname{atan2}\left(\hat{s}, \hat{c}\right), \tag{43}$$

where $\hat{c}$ and $\hat{s}$ are generated by the observer (41). Note also that

$$\sin\hat{\theta} = \frac{\hat{s}}{\sqrt{\hat{c}^2 + \hat{s}^2}}, \quad \cos\hat{\theta} = \frac{\hat{c}}{\sqrt{\hat{c}^2 + \hat{s}^2}}, \quad \tan\hat{\theta} = \frac{\hat{s}}{\hat{c}}. \tag{44}$$

Let us define $\zeta_\theta = \tan(\theta - \hat{\theta})$. By noting that $\zeta_c = c - \hat{c}$, $\zeta_s = s - \hat{s}$, and using the fact that $\tan\theta = \sin\theta/\cos\theta$, we have

$$\begin{aligned}\zeta_\theta &= \frac{\tan\theta - \tan\hat{\theta}}{1 + \tan\theta\tan\hat{\theta}} = \frac{\hat{c}\sin\theta - \hat{s}\cos\theta}{\hat{c}\cos\theta + \hat{s}\sin\theta} \\ &= \frac{(c - \zeta_c)\sin\theta - (s - \zeta_s)\cos\theta}{(c - \zeta_c)\cos\theta + (s - \zeta_s)\sin\theta} \\ &= \frac{\zeta_s\cos\theta - \zeta_c\sin\theta}{1 - \zeta_c\cos\theta - \zeta_s\sin\theta}.\end{aligned} \tag{45}$$

Since $\zeta_c(t)$ and $\zeta_s(t)$ converge to zero, we have $\zeta_\theta(t)$ converge to zero as $t \to \infty$, which directly implies the convergence of $\hat{\theta}$ to θ for the initial estimated orientation error satisfying $|\theta(0) - \hat{\theta}(0)| < \pi/2$.

IV. Simulations

In order to illustrate the effectiveness of the extended look-ahead controller and the observer, a number of simulations are performed. Additionally, the purpose of this simulation is to properly determine the control parameters for the experimental setup. First, we consider a scenario of 4 vehicles platoon, where all states (position and orientation) can be measured accurately and are not disturbed by noise. This allows us to investigate the optimal gains k_1 and k_2 and the effectiveness of the extended look-ahead controller against corner-cutting. Second, we consider a scenario of a 2 vehicles platoon where the second vehicle is controlled by extended look-ahead controller with the orientation-observer, in the presence and absence of noise. In this scenario, the performance of the observer is evaluated.

We consider a platoon of 4 vehicles, with the first vehicle controlled by the tracking controller of [16] to track a predefined eight-shaped trajectory, while the other vehicles controlled by the extended look-ahead controller to track their respective preceding vehicle. It should be noted that the first vehicle can also be directly controlled (simulating a driving scenario where the first vehicle is driven by a human), or controlled by other trajectory-tracking (e.g., [17]) or path-following controllers (e.g., [5]). The eight-shaped trajectory is generated by two-half circles with the radius 0.3 m and quintic polynomial functions. The controller performance to track a circular trajectory (constant curvature) as in [15] is also performed, but the eight-shaped trajectory is chosen since it also represents a combination of constant and varying curvatures. The reference curvature of the eight-shaped path is given in Fig. 8. The dimensions of the track are chosen in accordance with the experimental setup, which is presented in the next section. The first vehicle starts at initial position $(x, y) = (0.7, 0.5)$ m, maneuvering along the eight-shaped path. The other vehicles start at $(0.625, 0.425)$, $(0.55, 0.35)$, and $(0.475, 0.275)$ for vehicle 2, 3, and 4, respectively. All vehicles are initiated with $\upsilon = 0.06$ m/s and $\theta = 0.9707$ rad/s, and $d = 0.1$ m is chosen. The extended look-ahead controller gain is determined by an iterative manner and is equal for vehicle 2, 3, and 4. It should be noted that the choice for the proper gain is also determined by the available experimental arena and the reference trajectory. It is also worth noting that the higher gain value results in a faster convergence towards

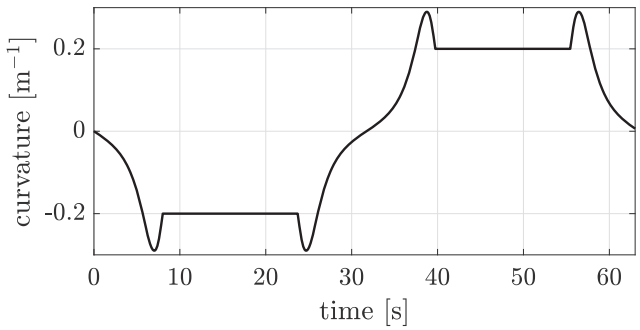

Fig. 8. Reference curvature for an eight-shaped path with $v = 0.06$ m/s.

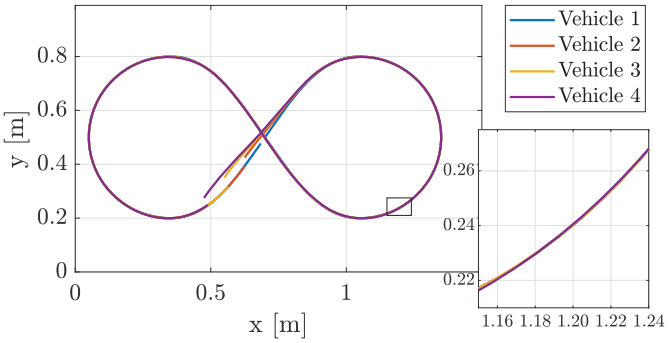

Fig. 9. Trajectory of 4-vehicles platoon tracking an eight-shaped path, with $k_1 = k_2 = 0.75$.

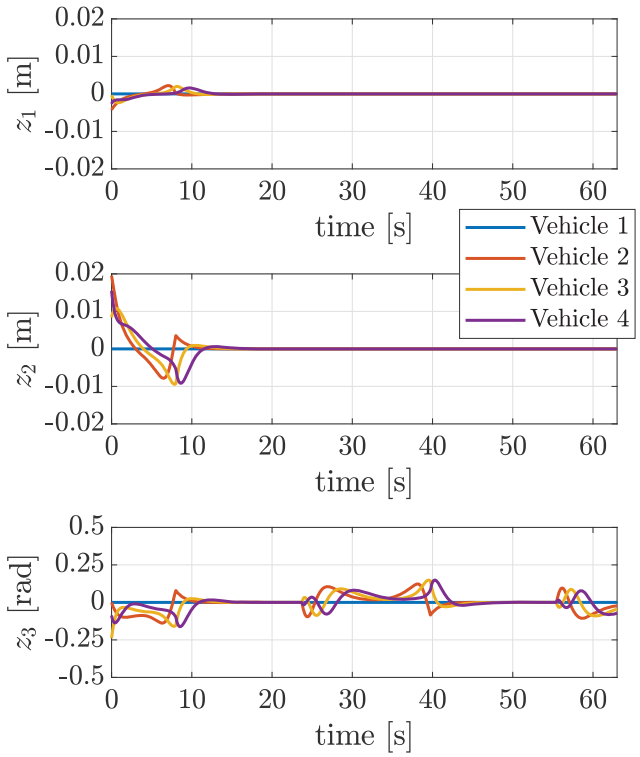

Fig. 10. Errors of a platoon with the extended look-ahead controller on an eight-shaped path.

the desired path. However, the higher gain value also results in a more sensitive response to the curvature change. In practical situation, this is undesirable since a slight change in states measurement (e.g., due to noise, sensor inaccuracy) could result in an over compensation. The trajectory of all vehicles with $k_1 = k_2 = 0.75$ is shown in Fig. 9. It can be observed that all vehicles in the platoon converges to the reference path and corners are not cut. This shows the advantage of our controller in comparison to the controller in [12], where corners with $\dot{\kappa}_r \neq 0$ are still cut. From Fig. 10, it can be observed that z_1 and z_2 converge to zero. On the other hand, the orientation error z_3 converges to zero if $\dot{\kappa}_r = 0$, which can be seen from $t = 11$ s until $t = 22$ s and from $t = 42$ s until $t = 55$ s. On the transition state when $\dot{\kappa}_r \neq 0$, z_3 is bounded given the condition that $\dot{\kappa}_r$ is small enough.

In the second scenario, we consider a platoon of 2 vehicles, with identical parameters as vehicle 1 and vehicle 2 in the previous simulation. A two-vehicles setting is used since we want to study the convergence of the estimated orientation to the true orientation of the follower vehicle. The first vehicle is controlled by the tracking controller [16], while the second vehicle is controlled by the extended look-ahead controller (17) with the observer (41). The initial condition of the observer states are set as $\hat{x}(0) = 0.625$, $\hat{y}(0) = 0.425$, and $\hat{\theta} = 0.8$ rad/s. It is assumed that the position can be measured accurately without any noise, while the orientation measurement is disturbed by a noise. The noise of the orientation sensor is simulated as a white noise with a power spectral density of 5×10^{-5}. For the observer gains, we select $l_1 = 10$, $l_2 = 10$, $l_3 = 1000$, and $l_4 = 1000$. First, we simulate the system without the observer, i.e., the control laws (17) are calculated using the orientation measured from the sensor with noise. Second, we simulate the system with the orientation-error observer, where the orientation is estimated based on the position sensor. We denote θ as the true orientation, $\hat{\theta}$ as the estimated orientation, and $\bar{\theta}$ as the orientation obtained from the sensor. The error plots of $\theta - \bar{\theta}$ (for the scenario without the observer) and $\theta - \hat{\theta}$ (for the scenario with the observer) are depicted in Fig. 11. It can be observed that for the scenario without the observer, the measured orientation (shown in gray line) is heavily disturbed by noise. On the other hand, the error $\theta - \hat{\theta}$ (shown in black line) is not disturbed by noise and converges to zero, which means that the estimated orientation $\hat{\theta}$ converges to the true orientation θ.

V. Experiments

In this section, we conduct an experiment to confirm the theoretical analyses and subsequent to the simulation results. This practical experiment is conducted also to provide an insight in how the parameters for our controller can be chosen to accommodate the slave controller in mobile robots. Furthermore, the purpose of this experiment is to verify the performance of the orientation-error observer in an experimental environment, where the orientation measurement is disturbed by noise due to inherent limitation of the sensor/vision system. The main components of this experimental setup are: four mobile robots (E-puck [26]), a PC, and a camera. A unique marker (2D barcode) is attached to each E-puck for identification, such that the orientation and the position of each E-puck can

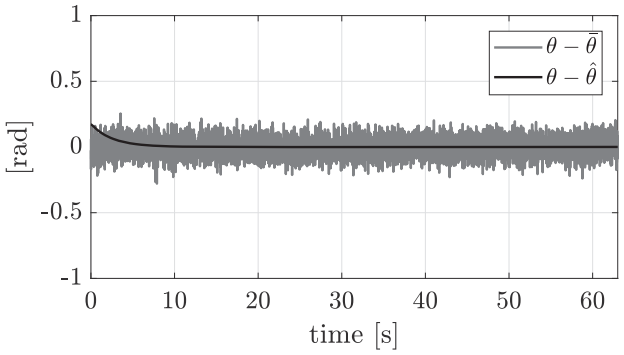

Fig. 11. Errors of $\theta - \hat{\theta}$ and $\theta - \bar{\theta}$, where θ is the true orientation, $\hat{\theta}$ is the estimated orientation, and $\bar{\theta}$ is the orientation obtained from the sensor with noise.

TABLE I
E-PUCK SPECIFICATION

Specification	Values
Robot radius	37 mm
Wheel radius (r)	20.5 mm
Axle length (L)	52 mm
Speed unit	0.00628 rad/s
Encoder resolution	159.23
Maximum angular speed	1000 units
Maximum velocity	13 cm/s
Maximum angular velocity	5 rad/s

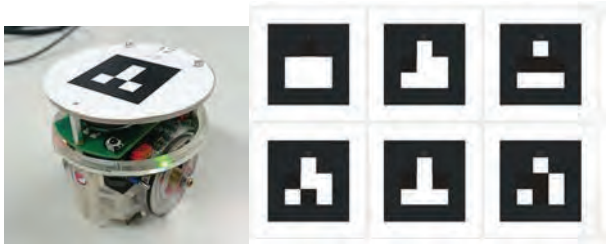

Fig. 12. The E-puck mobile robot and markers used for identification.

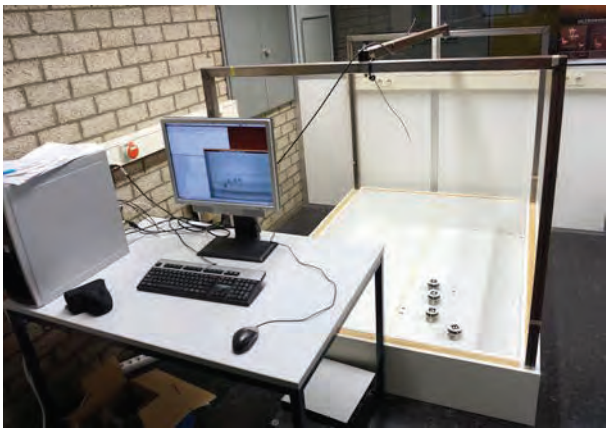

Fig. 13. The mobile robot experimental setup with E-pucks in the 1.75 × 1.28 m arena. The camera is attached to the frame to measure the position and orientation of the robots.

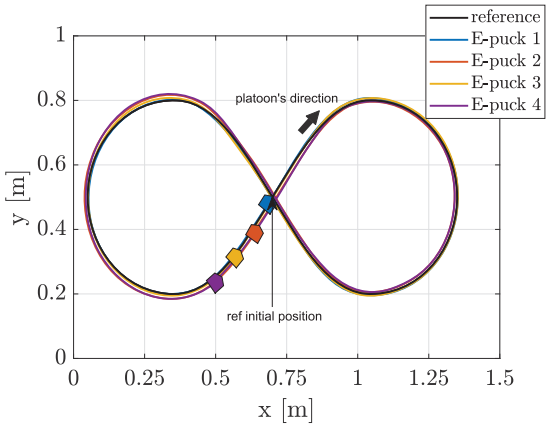

Fig. 14. Trajectory of E-pucks with extended look-ahead controller, where the orientation is measured directly from the camera.

be determined (see Fig. 12). The PC is used to generate a reference trajectory and to determine the absolute coordinates and orientations of the robots from the camera. The control algorithm is also computed in the PC, and is send directly to each E-puck via a Bluetooth protocol. The experimental setup is shown in Fig. 13. Since the E-puck is a differential-drive mobile robot, its motion is controlled by providing velocity inputs of the left and right wheels, denoted by v_l and v_r, respectively. The transformation of the linear and angular velocity, v and ω, to the individual wheels velocity can be determined using the following relation

$$v_l = v - \frac{\omega L}{2}, \quad v_r = v + \frac{\omega L}{2}, \tag{46}$$

where L is the length between the left and right wheel of E-puck, as given in Table I.

In order to support comparison of the simulation results presented in the previous section, for this experiment we use the identical eight-shaped reference trajectory as in the simulation. In the first experiment, we use the extended look-ahead controller without the observer, thus, the orientation of the mobile robots are obtained directly from the camera. The objectives of the first experiment are to study the effectiveness of the extended look-ahead controller, compared to the theoretical results presented in the previous section, to verify the suitable gain for the experiment, and to study the behavior of the system under the presence of measurement noises. In the second experiment, we apply the observer to estimate the orientation of the mobile robots. The objective of this second experiment is to study the effectiveness of the observer in practice, and to confirm the simulation results. All E-pucks are initiated with $v = 0.06$ m/s, with the controller gains $k_1 = k_2 = 0.75$ for both experiments, and with the observer gains $l_1 = 10$, $l_2 = 10$, $l_3 = 1000$, and $l_4 = 1000$ for the second experiment.

Fig. 14 shows the trajectory of robots with the extended look-ahead controller. It can be observed that the trajectory of all follower robots converge to the reference trajectory. Clearly, this experiment shows that the extended look-ahead controller effectively avoids corner-cutting. However, it can be seen that the follower vehicles start to deviate on the left side of the eight-shaped path, due to the inaccuracy (due to noise, or displacement of the 2D marker) in the orientation

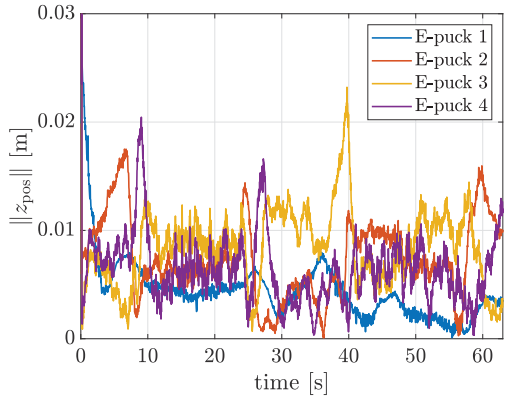

Fig. 15. 2-norm of the position error from experiments incorporating extended look-ahead controller without observer.

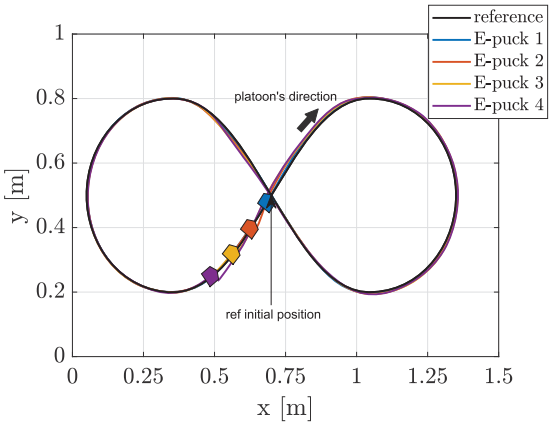

Fig. 16. Trajectory of E-pucks with extended look-ahead controller and an orientation observer. The orientation of each E-puck is estimated from the position.

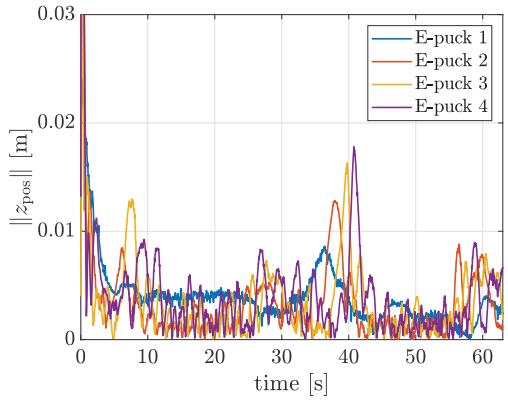

Fig. 17. 2-norm of the position error from experiments incorporating extended look-ahead controller with observer.

measurement. The 2-norm of the position error, define as $\sqrt{z_1^2 + z_2^2}$, is depicted in Fig. 15. It can be observed from this plot that E-puck 3 has the largest deviation, peaking at $t = 40$ s. To address this problem, the orientation-error observer is integrated to the extended-look-ahead controller in the second experiment. In Fig. 16, the trajectory of all robots with the extended look-ahead controller and orientation-error observer is shown. It can be seen directly that the tracking accuracy of all follower robots is improved, thus showing the effectiveness of the orientation-error observer. From Fig. 17, where the 2-norm of the position error is depicted, it can also be verified that the observer reduces the deviation caused by the inaccuracy of the orientation measurement. We may also notice some measurement noises on the position measurement, but they are small enough (less than 0.02 m) and can be safely neglected.

VI. Conclusion

This paper presents a novel extended look-ahead controller in vehicle platooning. The look-ahead target point is extended to a virtual point induced from the position and the curvature of the reference vehicle, thus ensuring a better tracking performance at cornering, preventing corner-cutting behavior. A stability result on the internal dynamics is presented, showing that the closed-loop system is stable under the given bound of the reference curvature and the initial relative position and orientation of the vehicles. The simulation results show that the proposed approach improves the tracking performance at cornering, ensuring that the corners are not cut. To address the orientation measurement noise in the experiment, an orientation-error observer is also designed. The effectiveness of the integrated extended look-ahead controller and orientation-error observer is further validated by means of experiment with a platoon consisting of four E-pucks. The experimental results confirm that the application of the extended look-ahead controller in vehicle platooning compensates for corner-cutting, and also confirm that the observer reduces the noise presents in the orientation measurement. The continuation of this paper is to extend the approach to the single-track model, as an important step towards the application of our controller in a real vehicle. To adapt our controller to a single-track dynamic model with tire forces, we can design a slave controller that controls acceleration or speed, internally compensating for the vehicle mass. The stability of the real vehicle can be guaranteed by other controllers (Electronic Stability Control (ESC), or Anti-Lock Braking System (ABS), for instance), and our controller can be used in conjunction with those other controllers. In conclusion, the application of our controller to the real vehicle may poses additional conditions, but is feasible.

Appendix A

In this appendix we show the derivation in obtaining the equilibrium point of δ. Consider $\delta = \theta - \theta_r + \alpha_r$, as in (14). By differentiating it with respect to time, we obtain

$$\dot{\delta} = \omega - \omega_r + \dot{\alpha}_r. \tag{47}$$

Substituting ω as in (17) and (7) into (47) eventually yields

$$\dot{\delta} = -(1 - \cos\delta)\,\omega_r - \frac{v_r}{d}\sin\delta + \zeta_r, \tag{48}$$

where

$$\zeta_r = \frac{k_1 \sin\delta}{d} z_1 - \frac{k_2 \cos\delta}{d} z_2 + \left(\frac{h_{\kappa,1}}{d}\sin\delta - \frac{h_{\kappa,2}}{d}\cos\delta + \frac{2d}{\sqrt{4 - d^2\kappa_r^2}}\right)\dot{\kappa}_r, \tag{49}$$

(z_1, z_2) as in (12), and $(h_{\kappa,1}, h_{\kappa,2})$ as in (16). In a steady state condition, which implies that $z_1 = z_2 = 0$ and $\dot{\kappa}_r = 0$, we have

$$\dot{\delta} = -(1-\cos\delta)\,\omega_r - \frac{v_r}{d}\sin\delta. \tag{50}$$

By noting that $\kappa_r = \omega_r / v_r$ and $\sin^2\delta = 1-\cos^2\delta$, the equilibrium points of (50) are determined by

$$\left(1+d^2\kappa_r^2\right)\cos^2\delta - 2d^2\kappa_r^2\cos\delta + \left(d^2\kappa_r^2 - 1\right) = 0,$$

and given by

$$\delta^\star = 2n\pi \tag{51}$$

$$\delta^\star = \arctan\left(\frac{-2d\kappa_r}{d^2\kappa_r^2-1}\right) + 2n\pi, \tag{52}$$

where $n = 0, \pm1, \pm2, \ldots$.

APPENDIX B

In this appendix we show how β is derived mathematically, such that z_3 has equilibrium points at $[0, \pi]$. Consider

$$z_3 = \theta - \theta_r + \alpha_r + \beta, \tag{53}$$

where $\beta : [-2\pi, 2\pi] \to [-1, 1]$. Taking the input ω as in (17) into account, the derivative of z_3 is given by

$$\begin{aligned}\dot{z}_3 = &-\frac{1}{d}\sin(\theta-\theta_r+\alpha)\left(-k_1 z_1 + v_r - \dot{\kappa}_r h_{\kappa,1}\right)\\ &+\frac{1}{d}\cos(\theta-\theta_r+\alpha)\left(-k_2 z_2 + d\omega_r - \dot{\kappa}_r h_{\kappa,2}\right)\\ &-\omega_r + \dot{\alpha}_r + \dot{\beta}.\end{aligned} \tag{54}$$

In the equilibrium we have

$$\dot{z}_3 = -\frac{v_r}{d}\sin(z_3-\beta) + \omega_r\cos(z_3-\beta) - \omega_r, \tag{55}$$

and we want $\dot{z}_3 = 0$ for $z_3 = 0$ and $z_3 = \pi$, i.e.,

$$\begin{aligned} z_3 = 0 \quad &\Rightarrow \sin\beta = -d\kappa_r\cos\beta + d\kappa_r\\ z_3 = \pi \quad &\Rightarrow \sin\beta = -d\kappa_r\cos\beta - d\kappa_r\end{aligned}$$

which can be rewritten as

$$\sin\beta = d\kappa_r\cos z_3 - d\kappa_r\cos\beta. \tag{56}$$

By substituting (53) into (56), and noting that $\delta = \theta - \theta_r + \alpha_r$, we have

$$\begin{aligned}\sin\beta &= d\kappa_r(\cos\delta\cos\beta - \sin\delta\sin\beta - \cos\beta)\\ \sin\beta(1+d\kappa_r\sin\delta) &= \cos\beta(d\kappa_r\cos\delta - d\kappa_r)\\ \frac{\sin\beta}{\cos\beta} &= \frac{d\kappa_r\cos\delta - d\kappa_r}{1+d\kappa_r\sin\delta},\end{aligned} \tag{57}$$

resulting in $\sin\beta$ and $\cos\beta$ as in (21a) and (21b).

APPENDIX C

In this section the claim on the boundedness of $\bar{v}_r$ and ξ_r is proven.

Proof: First we want to show the lower and upper bound of $\bar{v}_r$. We can rewrite (29) as

$$\begin{aligned}\Delta &= d^2\kappa_r^2(1-\cos\delta)^2 + (1+d\kappa_r\sin\delta)^2\\ &= 2d^2\kappa_r^2(1-\cos\delta) + 2d\kappa_r\sin\delta + 1. &(58)\\ &= 2d^2\kappa_r^2 + 1 + 2\left(d\kappa_r\sin\delta - d^2\kappa_r^2\cos\delta\right). &(59)\end{aligned}$$

To obtain the lower- and upper-bound of Δ, let us define an angle γ, characterized by $\sin\gamma = d\kappa_r/\sqrt{d^2\kappa_r^2+1}$ and $\cos\gamma = 1/\sqrt{d^2\kappa_r^2+1}$ such that we can write (59) as

$$\begin{aligned}\Delta &= 2d^2\kappa_r^2 + 1 + 2d\kappa_r\sqrt{d^2\kappa_r^2+1}\,(\cos\gamma\,\sin\delta - \sin\gamma\,\cos\delta)\\ &= 2d^2\kappa_r^2 + 1 + 2d\kappa_r\sqrt{d^2\kappa_r^2+1}\,(\sin(\delta-\gamma)).\end{aligned}$$

Since $|\sin(\delta-\gamma)| \le 1$, we have

$$\begin{aligned}\Delta &\ge 2d^2\kappa_r^2 + 1 - 2\left|d\kappa_r\sqrt{d^2\kappa_r^2+1}\right| \text{ and}\\ \Delta &\le 2d^2\kappa_r^2 + 1 + 2\left|d\kappa_r\sqrt{d^2\kappa_r^2+1}\right|\\ &\Rightarrow 3-2\sqrt{2} \le \Delta \le 3+2\sqrt{2},\end{aligned} \tag{60}$$

as the lower- and upper-bound of Δ, where the extreme value is obtained for $|d\kappa_r| = 1$. To show that $N > 0$, note that we can rewrite (28) as

$$N = \frac{1}{4}d^2\kappa_r^2(3-\cos\delta)(1-\cos\delta) + \left(1+\frac{1}{2}d\kappa_r\sin\delta\right)^2. \tag{61}$$

Since $N > 0$, by taking (58) into account, we can also rewrite (28) as

$$\begin{aligned}N &= \sqrt{\left(d^2\kappa_r^2(1-\cos\delta) + d\kappa_r\sin\delta + 1\right)^2}\\ &= \sqrt{\Delta + \left(d^2\kappa_r^2(1-\cos\delta) + d\kappa_r\sin\delta\right)^2}.\end{aligned} \tag{62}$$

Moreover, since $\Delta > 0$ (which follows directly from (29)), by substituting (62) into (26) we obtain

$$\begin{aligned}\bar{v}_r &= v_r\sqrt{1+\frac{1}{\Delta}\left(d^2\kappa_r^2(1-\cos\delta) + d\kappa_r\sin\delta\right)^2}\\ &= v_r\sqrt{1+\frac{(N-1)^2}{\Delta}} \ge v_r,\end{aligned} \tag{63}$$

which is the lower bound of $\bar{v}_r$. Note also that by using (58), we can rewrite N as

$$N = \frac{1}{2}(\Delta+1). \tag{64}$$

By substituting (64) into (63), and taking the upper bound of Δ in (60) into account, we eventually obtain

$$\bar{v}_r = v_r\sqrt{\frac{(\Delta+1)^2}{4\Delta}} \le v_r\sqrt{2}, \tag{65}$$

which is the upper bound of $\bar{v}_r$.

To show the upper bound of ξ_r, note that we can rewrite N/Δ as

$$\begin{aligned}\frac{N}{\Delta} &= \frac{d^2\kappa_r^2\,(1-\cos\delta)+d\kappa_r\sin\delta+1}{2d^2\kappa_r^2\,(1-\cos\delta)+2d\kappa_r\sin\delta+1}\\ &= \tfrac{1}{2}\left(1+\tfrac{1}{\Delta}\right) \le \tfrac{1}{2}\left(1+\tfrac{1}{\Delta^{\min}}\right)\\ &\le \tfrac{1}{2}\left(1+\tfrac{1}{3-2\sqrt{2}}\right) = \frac{2-\sqrt{2}}{3-2\sqrt{2}} = 2+\sqrt{2}, \qquad (66)\end{aligned}$$

where we use the lower bound of Δ in (60). Moreover, we also have

$$|g_\kappa| = \left|\frac{N}{\Delta}\,f_r\,(\delta,d,\kappa_r) - \frac{d\,(1-\cos\delta)}{\Delta}\right| < \frac{7}{9}d, \qquad (67)$$

where the bound on $|g_\kappa|$ is obtained by evaluating the function and the maximum value is obtained for $\kappa_r = 1/d$ and $\delta = \frac{3}{4}\pi$. By using the triangle inequality and substituting (66), (67) into (27), we have

$$\begin{aligned}\xi_r &= \frac{N}{\Delta d}\begin{bmatrix}\sin\delta & -\cos\delta\end{bmatrix}\begin{bmatrix}k_1 z_1\\ k_2 z_2\end{bmatrix} + g_\kappa\dot{\kappa}_r\\ |\xi_r| &\le \tfrac{2+\sqrt{2}}{d}\,(k_1\,|z_1| + k_2\,|z_2|) + \tfrac{7}{9}d\,|\dot{\kappa}_r|\,, \qquad (68)\end{aligned}$$

which is the bound of $|\xi_r|$. ■

APPENDIX D

Proof of Proposition 2: From (19), we have $\|z_{12}(t)\| \le \|z_{12}(0)\|$. Since $|\dot{\kappa}_r(t)| \le K$, from (33) we have

$$\begin{aligned}|\xi_r(t)| &\le \tfrac{2+\sqrt{2}}{d}\sqrt{k_1^2+k_2^2}\,\|z_{12}(t)\| + \tfrac{7d}{9}K\\ &\le \tfrac{2+\sqrt{2}}{d}\sqrt{k_1^2+k_2^2}\,\|z_{12}(0)\| + \tfrac{7d}{9}K\\ &\le \tfrac{v_r^{\min}}{d}\varepsilon + \tfrac{7d}{9}K =: \xi_r^{\max}, \qquad (69)\end{aligned}$$

where we use (34). Consider a positive-definite function

$$V_3(z_3) = 1-\cos z_3. \qquad (70)$$

The time derivative of $V_3(z_3)$ along the trajectory (24), by taking (32) into account, is given by

$$\begin{aligned}\dot{V}_3\,(z_3) &= -\frac{\bar{v}_r}{d}\sin^2 z_3 + \xi_r\sin z_3\\ &\le -\frac{v_r}{d}\sin^2 z_3 + |\xi_r|\,|\sin z_3|\\ &\le -\tfrac{v_r^{\min}}{2d}\left[\sin^2 z_3 + \left(|\sin z_3| - \tfrac{d}{v_r^{\min}}\,|\xi_r|\right)^2 - \left(\tfrac{d}{v_r^{\min}}\,|\xi_r|\right)^2\right]\\ &\le -\tfrac{v_r^{\min}}{2d}\left[\sin^2 z_3 - \left(\tfrac{d}{v_r^{\min}}\,|\xi_r|\right)^2\right]. \qquad (71)\end{aligned}$$

Let us define $\Omega_u = \{z_3 \in \mathbb{R}\,|\,|\sin z_3| \le \frac{d}{v_r^{\min}}\xi_r^{\max}\}$, where $\xi_r^{\max}$ is as defined in (69). By noting that $|\xi_r(t)| \le \xi_r^{\max}$, solutions starting outside Ω_u move in the direction of decreasing V_3, since $\dot{V}_3 < 0$ outside Ω_u, and eventually will be inside and cannot leave Ω_u as $t \to \infty$, which corresponds to (35) when substituting $\xi_r^{\max}$ from (69) in the definition for Ω_u. This proves claim (a).

Moreover, for

$$\lim_{t\to\infty} z_1(t) = 0, \quad \lim_{t\to\infty} z_2(t) = 0, \quad \lim_{t\to\infty}\dot{\kappa}_r(t) = 0,$$

we have $\xi_r(t) \to 0$ as $t \to \infty$, according to (33). From claim (a), we have that any solution of z_3 will be inside and cannot leave Ω_u as $t \to \infty$, which means that $\sin z_3(t) \to \frac{d}{v_r^{\min}}\xi_r(t)$ as $t \to \infty$. Since $d > 0$, $v_r^{\min} > 0$, we have $\sin z_3(t)$ converges to zero if and only if $\xi_r(t)$ converges to zero, hence proving claim (b).

It is important to note that for a platoon with more than 2 vehicles, $v(t)$ will become the reference for the next vehicle. Thus, we also need the condition of $v(t) \ge v^{\min} > 0$. From (37) we have $|\sin z_3(0)| \le \frac{7}{18} - \frac{8}{27}\varepsilon$, so using (38), we start in the set Ω_u and stay in the set Ω_u, which implies $|\sin z_3(t)| \le \frac{7}{18} - \frac{8}{27}\varepsilon$ and $\cos z_3(t) \ge \sqrt{1-\left(\frac{7}{18}-\frac{8}{27}\varepsilon\right)^2} > 0$ for all $t \ge 0$.

From (17), we have

$$\begin{aligned}v = v_r\,(\cos\delta + d\kappa_r\sin\delta) &- (k_1 z_1\cos\delta + k_2 z_2\sin\delta)\\ &- \dot{\kappa}_r\left(h_{\kappa,1}\cos\delta + h_{\kappa,2}\sin\delta\right). \qquad (72)\end{aligned}$$

Let us denote $\eta := \cos\delta + d\kappa_r\sin\delta$. Note that by using (22) we have

$$\begin{aligned}\eta &= \cos z_3\sqrt{d^2\kappa_r^2\,(1-\cos\delta)^2 + (1+d\kappa_r\sin\delta)^2}\\ &= \cos z_3\sqrt{2d\kappa_r\,(d\kappa_r - d\kappa_r\cos\delta + \sin\delta) + 1}\\ &= \sqrt{2d\kappa_r\sin z_3\cos z_3\eta + \cos^2 z_3}. \qquad (73)\end{aligned}$$

By noting that $|\kappa_r| < 1/d$, we solve (73) with respect to η as

$$\begin{aligned}\eta &= \cos z_3\left(d\kappa_r\sin z_3 + \sqrt{d^2\kappa_r^2\sin^2 z_3 + 1}\right)\\ &\ge \left(-1+\sqrt{2}\right)\cos z_3. \qquad (74)\end{aligned}$$

Moreover, from (16) we have

$$|h_{\kappa,1}| \le \tfrac{d^2}{2\sqrt{3}} =: h_{\kappa,1}^{\max} \qquad (75a)$$

$$|h_{\kappa,2}| \le d^2\left(\tfrac{4-\sqrt{3}}{2\sqrt{3}}\right) =: h_{\kappa,2}^{\max}. \qquad (75b)$$

Thus, from (72), by substituting (37), (38), and (75), we obtain

$$\begin{aligned}v(t) &\ge v_r\left(-1+\sqrt{2}\right)\cos z_3(t) - \sqrt{k_1^2+k_2^2}\,\|z_{12}(t)\|\\ &\quad - K\sqrt{\left|h_{\kappa,1}^{\max}\right|^2 + \left|h_{\kappa,2}^{\max}\right|^2}\\ &\ge v_r^{\min}\left(-1+\sqrt{2}\right)\sqrt{1-\left(\tfrac{7}{18}-\tfrac{8}{27}\varepsilon\right)^2} - \tfrac{v_r^{\min}\varepsilon}{2+\sqrt{2}}\\ &\quad - v_r^{\min}\left(\tfrac{1}{2}-\tfrac{5}{3}\varepsilon\right)\sqrt{\tfrac{5-2\sqrt{3}}{3}}\\ &\ge \varepsilon v_r^{\min}, \qquad (76)\end{aligned}$$

i.e., for $|\dot{\kappa}_r(t)| \le K$, where K is given in (38), we have $v(t) \ge \varepsilon v_r^{\min} > 0$. Moreover, due to $\cos z_3(t) \ge \sqrt{1-\left(\frac{7}{18}-\frac{8}{27}\varepsilon\right)^2} > 0$ for all $t \ge 0$, we can guarantee that $z_3(t)$ does not converge to π. Thus, the claim of $\sin z_3(t) \to 0$ also implies that $z_3(t) \to 0$ (modulo 2π), as $t \to \infty$. This proves claim (c). ■

APPENDIX E

Proof of Proposition 3: Let $\zeta = (\zeta_x, \zeta_y, \zeta_c, \zeta_s)$. Differentiating the positive definite Lyapunov function candidate

$$V_1\,(\zeta) = \frac{l_3}{2}\zeta_x^2 + \frac{l_4}{2}\zeta_y^2 + \frac{1}{2}\zeta_c^2 + \frac{1}{2}\zeta_s^2, \qquad (77)$$

along solutions of (42) results in

$$\begin{aligned}\dot{V}_1(\zeta) &= l_3\zeta_x v\zeta_c - l_1 l_3\zeta_x^2 + l_4\zeta_y v\zeta_s - l_2 l_4\zeta_y^2 \\ &\quad - \omega\zeta_c\zeta_s - l_3 v\zeta_x\zeta_c + \omega\zeta_c\zeta_s - l_4 v\zeta_y\zeta_s \\ &= -l_1 l_3\zeta_x^2 - l_2 l_4\zeta_y^2 \leq 0, \end{aligned} \tag{78}$$

which is negative semi-definite. We can conclude that the origin of (42) is uniformly globally stable (UGS). We can not only conclude that ζ_x, ζ_y, ζ_c, and ζ_s are bounded, but using (42) that also $\dot{\zeta}_x$, $\dot{\zeta}_y$, $\dot{\zeta}_c$, and $\dot{\zeta}_s$ are bounded, and therefore also $\ddot{\zeta}_x$, and $\ddot{\zeta}_y$ (which follows by differentiating (42), and by using the fact that $\dot{v}$ and $\dot{\omega}$ are bounded).

Differentiating the bounded function

$$V_2(\zeta) = -\dot{\zeta}_x\zeta_x - \dot{\zeta}_y\zeta_y \tag{79}$$

along the solutions of (42) results in

$$\begin{aligned}\dot{V}_2(\zeta) &= -\ddot{\zeta}_x\zeta_x - (v\zeta_c - l_1\zeta_x)^2 - \ddot{\zeta}_y\zeta_y - \left(v\zeta_s - l_2\zeta_y\right)^2 \\ &= -v^2\left(\zeta_c^2 + \zeta_s^2\right) + 2l_1 v\zeta_c\zeta_x + 2l_2 v\zeta_s\zeta_y \\ &\quad - l_1^2\zeta_x^2 - l_2^2\zeta_y^2 - \ddot{\zeta}_x\zeta_x - \ddot{\zeta}_y\zeta_y \\ &\leq -v_{\min}^2\left(\zeta_c^2 + \zeta_s^2\right) + M_x|\zeta_x| + M_y\left|\zeta_y\right|, \end{aligned} \tag{80}$$

for certain constants M_x and M_y, where we used the previously derived boundedness of signals. Using Matrosov's theorem ([27, Theorem 1], cf. [28, Theorem 2]), we can conclude that (42) is UGAS. ■

REFERENCES

[1] J. Ploeg, B. T. M. Scheepers, E. van Nunen, N. van de Wouw, and H. Nijmeijer, "Design and experimental evaluation of cooperative adaptive cruise control," in *Proc. 14th Int. IEEE Conf. Intell. Transp. Syst. (ITSC)*, Oct. 2011, pp. 260–265.

[2] S. Sheikholeslam and C. A. Desoer, "A system level study of the longitudinal control of a platoon of vehicles," *J. Dynamic Syst., Meas., Control*, vol. 114, no. 2, pp. 286–292, Jun. 1992.

[3] P. Morin and C. Samson, "Motion control of wheeled mobile robots," in *Springer Handbook of Robotics*. Berlin, Germany: Springer-Verlag, 2008, pp. 799–826.

[4] R. Rajamani, H.-S. Tan, B. K. Law, and W.-B. Zhang, "Demonstration of integrated longitudinal and lateral control for the operation of automated vehicles in platoons," *IEEE Trans. Control Syst. Technol.*, vol. 8, no. 4, pp. 695–708, Jul. 2000.

[5] J. Plaskonka, "Different kinematic path following controllers for a wheeled mobile robot of (2,0) type," *J. Intell. Robotic Syst.*, vol. 77, nos. 3–4, pp. 481–498, Mar. 2015.

[6] E. Lefeber, J. Ploeg, and H. Nijmeijer, "A spatial approach to control of platooning vehicles: Separating path-following from tracking," *IFAC-Papers OnLine*, vol. 50, no. 1, pp. 15000–15005, Jul. 2017.

[7] S. Solyom, A. Idelchi, and B. B. Salamah, "Lateral control of vehicle platoons," in *Proc. IEEE Int. Conf. Syst., Man, Cybern.*, Oct. 2013, pp. 4561–4565.

[8] S. E. Shladover *et al.*, "Automated vehicle control developments in the PATH program," *IEEE Trans. Veh. Technol.*, vol. 40, no. 1, pp. 114–130, Feb. 1991.

[9] D. Swaroop, J. K. Hedrick, and S. B. Choi, "Direct adaptive longitudinal control of vehicle platoons," *IEEE Trans. Veh. Technol.*, vol. 50, no. 1, pp. 150–161, Jan. 2001.

[10] R. Rajamani and S. E. Shladover, "An experimental comparative study of autonomous and co-operative vehicle-follower control systems," *Transp. Res. C, Emerg. Technol.*, vol. 9, no. 1, pp. 15–31, 2001.

[11] C. C. de Wit, "Trends in mobile robot and vehicle control," in *Control Problems in Robotics and Automation*. London, U.K.: Springer-Verlag, 1998, pp. 151–175.

[12] P. Petrov, "Nonlinear adaptive control of a two-vehicle convoy," *Open & Systemics J.*, vol. 3, no. 2, pp. 70–78, 2009.

[13] A. Morales and H. Nijmeijer, "Merging strategy for vehicles by applying cooperative tracking control," *IEEE Trans. Intell. Transp. Syst.*, vol. 17, no. 12, pp. 3423–3433, Dec. 2016.

[14] A. Bayuwindra, O. L. Aakre, J. Ploeg, and H. Nijmeijer, "Combined lateral and longitudinal CACC for a unicycle-type platoon," *IEEE Intelligent Vehicles Symposium, Proceedings*, no. 4, pp. 527–532, 2016.

[15] A. Bayuwindra, J. Ploeg, E. Lefeber, and H. Nijmeijer, "Combined longitudinal and lateral control of car-like vehicle platooning with extended look-ahead," *IEEE Trans. Control Syst. Technol.*, to be published.

[16] Z. P. Jiang and H. Nijmeijer, "Tracking control of mobile robots: A case study in backstepping," *Automatica*, vol. 33, no. 7, pp. 1393–1399, Jul. 1997.

[17] Y. Kanayama, Y. Kimura, F. Miyazaki, and T. Noguchi, "A stable tracking control method for an autonomous mobile robot," in *Proc. IEEE Int. Conf. Robot. Autom.*, May 1990, vol. 30, no. 5, pp. 384–389.

[18] A. Loría and E. Panteley, "Cascaded nonlinear time-varying systems: Analysis and design," in *Advanced Topics in Control Systems Theory* (Lecture Notes in Control and Information Science). London, U.K.: Springer, 2005, pp. 23–64.

[19] E. Panteley, E. Lefeber, A. Loría, and H. Nijmeijer, "Exponential tracking control of a mobile car using a cascaded approach," *IFAC Proc. Vol.*, vol. 31, no. 27, pp. 201–206, Sep. 1998.

[20] H. K. Khalil, *Nonlinear Systems*, 3rd ed. Upper Saddle River, NJ, USA: Prentice-Hall, 2002.

[21] H. Nijmeijer and A. J. van der Schaft, *Nonlinear Dynamical Control Systems*. New York, NY, USA: Springer-Verlag, 1990.

[22] S. P. M. Noijen, P. F. Lambrechts, and H. Nijmeijer, "An observer-controller combination for a unicycle mobile robot," *Int. J. Control*, vol. 78, no. 2, pp. 81–87, 2005.

[23] J. Jakubiak, E. Lefeber, K. Tchon, and H. Nijmeijer, "Two observer-based tracking algorithms for a unicycle mobile robot," *Int. J. Appl. Math. Comput. Sci.*, vol. 12, no. 4, pp. 513–522, 2002.

[24] J. Jakubiak, H. Nijmeijer, and E. Lefeber, "Observer based tracking controllers for a mobile car," Eindhoven Univ. Technol., Eindhoven, The Netherlands, Tech. Rep., 1999.

[25] T. P. Beumer, "Control of platooning mobile robots: Experimental validation," M.S. thesis, Dept. Mech. Eng., Eindhoven Univ. Technol., Eindhoven, The Netherlands, 2017.

[26] F. Mondada and M. Bonani. (2007). *E-Puck Education Robot*. [Online]. Available: http://www.e-puck.org

[27] A. Lorìa, E. Panteley, D. Popovic, and A. R. Teel, "A nested Matrosov theorem and persistency of excitation for uniform convergence in stable nonautonomous systems," *IEEE Trans. Autom. Control*, vol. 50, no. 2, pp. 183–198, Feb. 2005.

[28] E. Lefeber, S. J. A. M. Van den Eijnden, and H. Nijmeijer, "Almost global tracking control of a quadrotor UAV on SE(3)," in *Proc. IEEE Conf. Decis. Control*, Dec. 2017, vol. 56, no. 3, pp. 1175–1180.

Anggera Bayuwindra received the B.Sc. and M.Sc. degrees in electrical engineering (specializing in control and intelligent system) from the Bandung Institute of Technology, Bandung, Indonesia, in 2006 and 2012, respectively. He is currently pursuing the Ph.D. degree with the Department of Mechanical Engineering, Eindhoven University of Technology, Eindhoven, The Netherlands. He was an Engineer with Infineon Technologies, Batam, Indonesia. His current research is on the nonlinear control system design, in particular the integrated longitudinal and lateral control for cooperative and automated vehicles.

Erjen Lefeber received the M.Sc. degree in applied mathematics and the Ph.D. degree in tracking control of nonlinear mechanical systems from the University of Twente, Enschede, The Netherlands, in 1996 and 2000, respectively. In 2015, he joined the Dynamics and Control Group, where he worked on modeling and control of manufacturing systems from 2000 to 2015. Since 2000, he has been an Assistant Professor with the Department of Mechanical Engineering, Eindhoven University of Technology. His current research is on nonlinear control theory, in particular the control of drones and the control of platooning vehicles.

Jeroen Ploeg received the M.Sc. degree in mechanical engineering from the Delft University of Technology, Delft, The Netherlands, in 1988, and the Ph.D. degree in mechanical engineering on the control of vehicle platoons from the Eindhoven University of Technology, Eindhoven, The Netherlands, in 2014. From 1989 to 1999, he was with Tata Steel, IJmuiden, The Netherlands, where his interest was in the development and implementation of dynamic process control systems for large-scale industrial plants. He was with TNO, Helmond, The Netherlands, from 1999 to 2017, as a Principal Scientist in the field of vehicle automation and road safety assessment. Since 2017, he has also been a part-time Associate Professor with the Mechanical Engineering Department, Eindhoven University of Technology, Eindhoven. He is currently with 2getthere, Utrecht, The Netherlands, where he leads the research and development activities in the field of cooperative automated driving for automated transit systems, in particular platooning. His research interests include control system design for cooperative and automated vehicles, in particular string stability of vehicle platoons, the design of interaction protocols for complex driving scenarios, and the motion control of wheeled mobile robots.

Henk Nijmeijer (F'00) was born in 1955. In January 2015, he was a Scientific Director of the Dutch Institute of Systems and Control (DISC). He is a Full Professor at Eindhoven, and he Chairs the Dynamics and Control Group. He has published a large number of journal and conference papers, and several books, and he is or was at the editorial board of numerous journals. He has been an IFAC Council Member since 2011. He is a member of the Mexican Academy of Sciences. He received the IEE Heaviside Premium in 1990. He was a recipient of the 2015 IEEE Control Systems Technology Award. He is appointed as an Honorary Knight of the Golden Feedback Loop (NTNU) in 2011. He is an Editor of *Communications in Nonlinear Science and Numerical Simulations*. He is a Graduate Program Director of the TU/e Automotive Systems program.